RSC Advances

PAPER

View Article Online
View Journal | View Issue

Cite this: *RSC Adv.*, 2025, **15**, 33884

Effective detection of acetone gas molecules using PLD deposited tungsten oxide microwires for biomedical applications

Sankar Ganesh Ramaraj, *[ad] Keying Huang,[a] Amal Musa Alrebh,[b] Meera Almansoori,[b] Chuanlai Zang,[c] Jiaqi Yang,[a] Md Shamim Sarker,[a] Hiroyasu Yamahara *[ac] and Hitoshi Tabata *[ac]

Received 4th July 2025
Accepted 21st August 2025

DOI: 10.1039/d5ra04753f

rsc.li/rsc-advances

Skin gas sensors offer a non-invasive route for monitoring biomarkers such as acetone, relevant to metabolic conditions like diabetes. In this study, WO_3 thin films were deposited on $LaAlO_3$ (100) substrates *via* pulsed laser deposition and evaluated for acetone sensing. X-ray diffraction analysis confirmed the formation of highly crystalline WO_3 thin films at 600 °C. Atomic force microscopy analysis revealed a uniform film morphology with nanoscale grain structures, emphasizing the role of grain size in enhancing the gas adsorption and diffusion. The amorphous films exhibited an excellent response at 300 °C, detecting concentrations as low as 100 ppb in an air atmosphere. In addition, the fabricated sensor exhibited rapid response (19 s) and recovery (20 s) times. Distinct sensing mechanisms were observed under dry and ambient air conditions, indicating the influence of humidity and oxygen species. These findings demonstrate the significance of substrate selection, deposition parameters, and post-annealing treatment in tuning the structural and functional properties of WO_3-based thin film gas sensors for ultra-low detection of acetone gas molecules.

1. Introduction

Diagnosing diseases through the analysis of exhaled breath and skin-emitted gases is gaining increased attention owing to its cost-effectiveness, rapid response, convenience, and non-invasive nature.[1–4] These bodily emissions contain thousands of volatile organic compounds (VOCs), some of which serve as specific biomarkers for various diseases. For instance, alkanes, alkenes, alcohols, aldehydes, and ketones have been linked to cancers and fatty liver diseases, while acetone, ammonia, and hydrogen sulphide/nitric oxide are indicative of diabetes, kidney disease, and asthma, respectively.[5–9] Diabetes mellitus is a chronic metabolic disorder caused by insufficient or dysregulated insulin levels in the blood. If left untreated, it can lead to serious complications such as vision loss, renal failure, ulcers, osteoporosis, and cardiovascular diseases. Under hyperglycemic conditions, acetone is produced in the liver *via* the decarboxylation of acetoacetate and dehydrogenation of isopropanol.[10–14] This acetone then enters the bloodstream and is expelled through the lungs during exhalation.[15] Recent studies have shown that breath and skin acetone concentration correlates strongly with blood glucose levels, making it a promising non-invasive biomarker for diabetes. Typically, healthy individuals exhibit breath acetone levels ranging from 300 to 900 parts per billion (ppb), whereas diabetic patients often present with significantly elevated concentrations.[16–20] Moreover, acetone levels are also influenced by fat metabolism and ketone body formation, making them valuable for diet and fitness monitoring. Considering the rising interest in non-invasive diagnostics, advanced sensing materials with high surface area and enhanced sensitivity capable of detecting acetone at ppb levels are imperative. Such developments are crucial for early-stage disease detection and personalized health monitoring.[21–25]

To meet these challenges, several gas sensing technologies have been explored, which utilize different methods to detect the gas molecules from breath and skin, such as Raman spectroscopy, electrochemical sensors, optical systems, surface acoustic wave devices, quartz crystal microbalances, gas chromatography, and semiconductor-based sensors.[26–32] Among these, metal-oxide semiconductor (MOS) sensors have shown considerable promise owing to their compact design, ease of integration, cost-effectiveness, and excellent sensitivity. Tungsten trioxide (WO_3), a widely studied n-type MOS material, is particularly attractive for gas sensing applications because of its nontoxic nature, high

[a]*Department of Bioengineering, Graduate School of Engineering, The University of Tokyo, 7-3-1 Hongo, Japan. E-mail: ramaraj@g.ecc.u-tokyo.ac.jp; yamahara@bioxide.t.u-tokyo.ac.jp; tabata@g.ecc.u-tokyo.ac.jp*

[b]*Department of Biomedical Engineering and Biotechnology, Undergraduate College of Medicine and Health Sciences, Khalifa University, Abu Dhabi, The United Arab Emirates*

[c]*Department of Electrical Engineering and Information Systems, Graduate School of Engineering, The University of Tokyo, 7-3-1 Hongo, Bunkyo-ku, Tokyo 113-8656, Japan*

[d]*Department of Materials Physics, Saveetha School of Engineering, Saveetha Institute of Medical and Technical Sciences, Thandalam, Chennai 602105, Tamil Nadu, India*

chemical stability, dangling bonds, chemical activity and favourable physicochemical properties.[33,34] With a tuneable bandgap ranging from 2.4 to 2.8 eV, WO_3 interacts effectively with gas molecules at elevated temperatures. Interestingly, numerous studies have investigated the gas sensing behavior of WO_3 in various morphologies and toward a wide range of target gases, as summarized below. For instance, acetone detection for breath analysis using Si-doped WO_3-based sensor materials has been reported, demonstrating enhanced thermal stability and selectivity, particularly for applications in diabetes diagnosis.[35] Qiao *et al.*, developed WO_3 nanostructures with various morphologies that were synthesized hydrothermally, among which the sea urchin-like WO_3 showed superior acetone sensing performance. It exhibited a high response of 2 to 100 ppm acetone with a rapid 3 s response time at 200 °C.[36] Hierarchical WO_3 phase junctions were synthesized *via* a tartaric acid-assisted hydrothermal method, with DL-tartaric acid yielding structures with highly exposed crystal facets. The resulting sensor exhibited excellent acetone sensing performance (R_a/R_g = 162.3 for 50 ppm), fast response/recovery times, and a low detection limit of 300 ppb at 180 °C.[37] Most WO_3-based sensors reported to date utilize the monoclinic γ-WO_3 phase; however, selective acetone detection has also been demonstrated using the less stable ε-WO_3 and faceted hexagonal phases.[38,39] Moreover, studies have revealed that morphology, crystal orientation, and grain size significantly influence the acetone sensing properties of WO_3.[40–43] Notably, the amorphous phase (a-WO_3) offers advantages over its crystalline counterpart, including higher surface area, structural flexibility, and superior chemical and corrosion resistance.[44–46] Given its potential for non-invasive diabetes diagnosis, understanding the underlying mechanisms behind the diverse and intriguing acetone sensing behaviors of WO_3 nanomaterials remains a critical research focus.

In this study, we investigate the performance of WO_3 microwire gas sensors, fabricated using electron beam lithography, for the efficient detection of acetone gas molecules. The WO_3 thin films were deposited using pulsed laser deposition (PLD), ensuring high uniformity and structural integrity. To better understand the growth behaviour, WO_3 films were deposited on different substrates and at various temperatures, with a focus on $LaAlO_3$ (100) substrates. This systematic approach allowed us to evaluate the effects of deposition parameters on film crystallinity, morphology, and surface uniformity, those are the key factors in optimizing gas sensing performance. We also extensively examined the optimal operating temperature, selectivity, and sensitivity (toward acetone) of the sensor. The results of this study provide a strong foundation for the development of WO_3-based gas sensors for non-invasive diabetes monitoring, where precise detection of acetone at low concentrations is of critical importance.

2. Experiment

2.1 Thin film deposition

WO_3 thin films were fabricated using the PLD technique. The deposition process utilized an ArF excimer laser operating at a frequency of 5 Hz, with the oxygen partial pressure maintained at 10 Pa. $LaAlO_3$ (100) substrates were selected owing to their small lattice mismatch with monoclinic γ-WO_3 (a = 3.77 Å), which facilitates strain-induced effects during film growth. The deposition temperature was systematically varied (200, 400, 600, 700 and 800 °C) to study its influence on the structural and morphological properties of the films. In addition, the WO_3 thin films were deposited on different substrate materials at 600 °C under identical conditions to compare the crystallinity and substrate influence on film growth.

2.2 WO_3 microwire fabrication

WO_3 microwires with a width of approximately 2 μm were fabricated using the top-down lithographic approach. The process began with cleaning the $LaAlO_3$/WO_3 thin film, deposited by PLD, in acetone and isopropanol, followed by spin-coating of OAP-HDMS adhesion promoter at 3000 rpm for 60 s and baking at 110 °C for 90 s. Subsequently, JSR-7790G photoresist was spin-coated at 3000 rpm for 30 s and baked under the same conditions. Microwire patterns were defined using a DWL66+ laser lithography system (405 nm). After development and rinsing with deionized water, the exposed WO_3 thin film over the patterned thin film was etched by reactive ion etching RIE using CF_4 gas at a flow rate of 20 sccm, pressure of 5 Pa, and RF power of 100 W for 1 min. The remaining photoresist was removed by cleaning with acetone and isopropanol. Finally, Au/Cr electrodes were patterned using laser lithography and deposited *via* radio frequency/direct

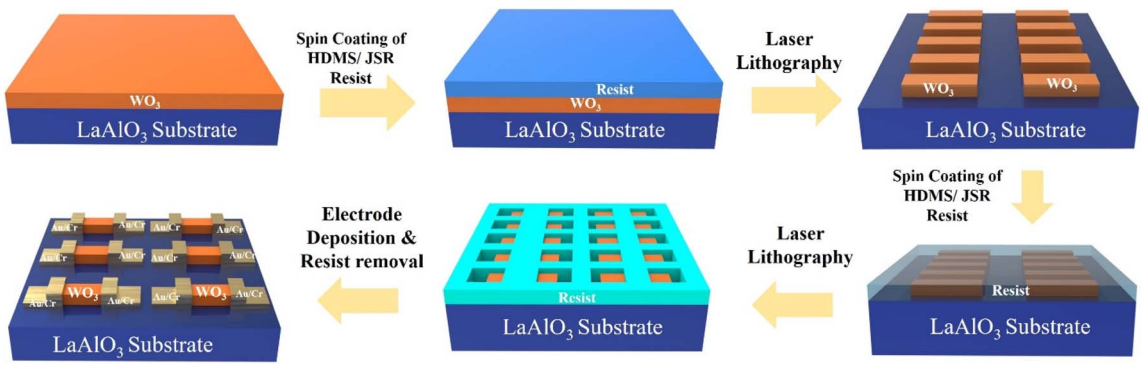

Fig. 1 Schematic of the preparation steps of the WO_3 microwire-based gas sensor.

current sputtering. A detailed schematic of the fabrication process is illustrated in Fig. 1.

2.3 Characterization

The chip die was prepared by laser dicing (Stealth dicer DISCO DFL7340). The pattern fabrication process was conducted by lithography (EB lithography ADVANTEST F7000S-VD02 system). Cr/Au electrode was deposited by sputtering (S-QAM, ULVAC Inc., Japan). The crystal structure and crystallinity were investigated by X-ray diffraction 2θ–ω scanning, ω scanning, and reciprocal space mapping using a four-circle diffractometer (Empyrean, PANalytical). The morphological features of the fabricated microwire were observed using scanning electron microscopy (SEM; S-4800, Hitachi High-Technologies Co., Japan). The chemical composition was analysed using energy dispersive X-ray spectroscopy (Inca Energy for JSM).

3. Results and discussion

The structure of the WO_3 thin films was characterised by X-ray diffraction (XRD) in the 2θ range of 20 to 80°. Fig. 2a shows the XRD patterns of the WO_3 thin films deposited at different temperatures. The crystallinity of the WO_3 thin films deposited on $LaAlO_3$ (100) substrates (laser frequency: 5 Hz; oxygen pressure: 10 Pa) clearly depends on the deposition temperature. The films deposited below 500 °C exhibit broad and weak diffraction peaks, indicating an amorphous or poorly crystallized structure. With increase in the temperature, particularly beyond 500 °C, distinct reflections corresponding to the WO_3 (200) plane become evident, suggesting improved crystallinity.[46–49] At 600 °C, the films show sharp and well-defined diffraction peaks, suggesting that this temperature is optimal for the growth of highly crystalline WO_3 on $LaAlO_3$ substrates. At 700 and 800 °C, the XRD peaks are sharp and intense, indicating high crystallinity and significant grain growth. The average crystallite size (D) was estimated using the Scherrer equation, $D = \frac{K\lambda}{\beta \cos \theta}$, where K is the shape factor (0.9), λ is the X-ray wavelength (0.154 nm for Cu Kα), β is the full width at half maximum (FWHM) in radians, and θ is the Bragg angle. The crystallite size increased from ~8 nm at 400 °C to ~38 nm at 800 °C, suggesting significant grain growth with higher annealing temperature.[50,51] The XRD patterns of the WO_3 thin films

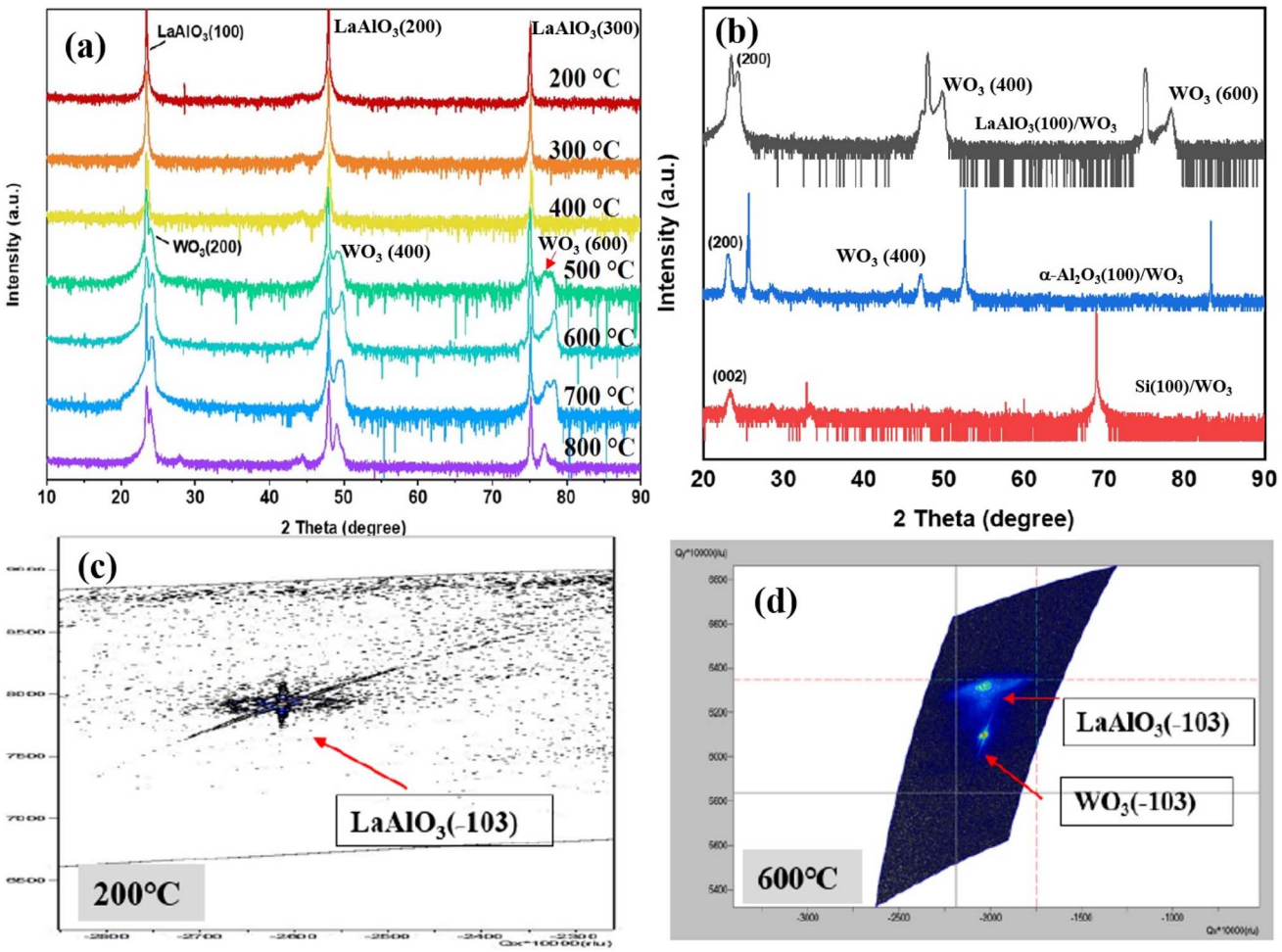

Fig. 2 X-ray diffraction patterns of the WO_3 thin films deposited (a) at different temperatures on $LaAlO_3$ (100) substrates and (b) on different substrates at 600 °C. Reciprocal space maps of the WO_3 thin films deposited on $LaAlO_3$ (100) substrates at (c) 200 °C and (d) 600 °C.

deposited on $LaAlO_3$ (100), Si (100), and α-Al_2O_3 ($0\bar{1}12$) substrates under identical conditions (600 °C, 5 Hz, 10 Pa O_2) highlight the influence of substrate on film crystallinity (Fig. 2b). The films on $LaAlO_3$ exhibit the sharpest and most intense peaks, indicating superior crystallinity. This is attributed to minimal lattice mismatch, which promotes epitaxial growth. In contrast, the films on α-Al_2O_3 show broader, less intense peaks, reflecting poorer crystallinity attributed to significant lattice mismatch and reduced structural compatibility. Reciprocal space mapping was conducted to assess the crystallinity and epitaxial relationship of the WO_3 thin films deposited on the $LaAlO_3$ (100) substrates at 200 and 600 °C. As shown in Fig. 2c, the reciprocal space map at 200 °C shows only the $LaAlO_3$ (−103) substrate peak, with no detectable WO_3 reflections, indicating that the film remains amorphous with no long-range crystalline order at this temperature. In contrast, the reciprocal space map at 600 °C (Fig. 2d) reveals distinct diffraction peaks corresponding to WO_3 (−103) and $LaAlO_3$ (−103) lattice planes.[52,53] The appearance of well-defined WO_3 peaks and their alignment with those of $LaAlO_3$ in the reciprocal space confirm a coherent epitaxial relationship between the film and substrate. This suggests that the WO_3 film adopts the in-plane atomic arrangement and orientation of the $LaAlO_3$ substrate, demonstrating successful epitaxial growth at elevated temperatures.[50,51] Fig. 3a and b show the SEM images of the WO_3 microwire; the one-dimensional morphology with a high aspect ratio indicates the successful fabrication of the microwire structures. The enlarged image (Fig. 3b) reveals smooth surfaces with a slightly porous texture, suggesting a well-defined microstructure with potential for enhanced surface activity. Fig. 4 illustrates the atomic force microscopy (AFM) images of the samples deposited at different temperatures, highlighting the evolution of the surface morphology. At 200 °C, the film exhibits a granular texture with pronounced peaks and valleys, resulting in a relatively high surface roughness of 9.76 nm (Fig. 4a and a1). This is attributed to limited adatom mobility at

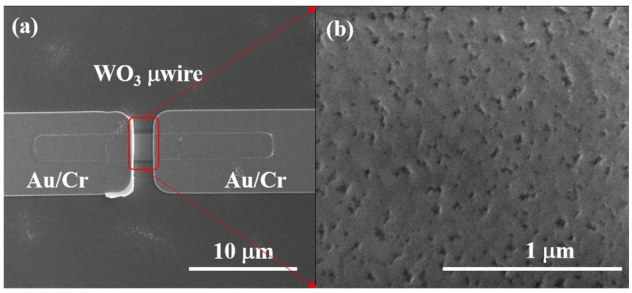

Fig. 3 Low-magnification scanning electron microscope image of the WO_3 microwires fabricated at 600 °C and (b) enlarged image of the red-highlighted area in (a).

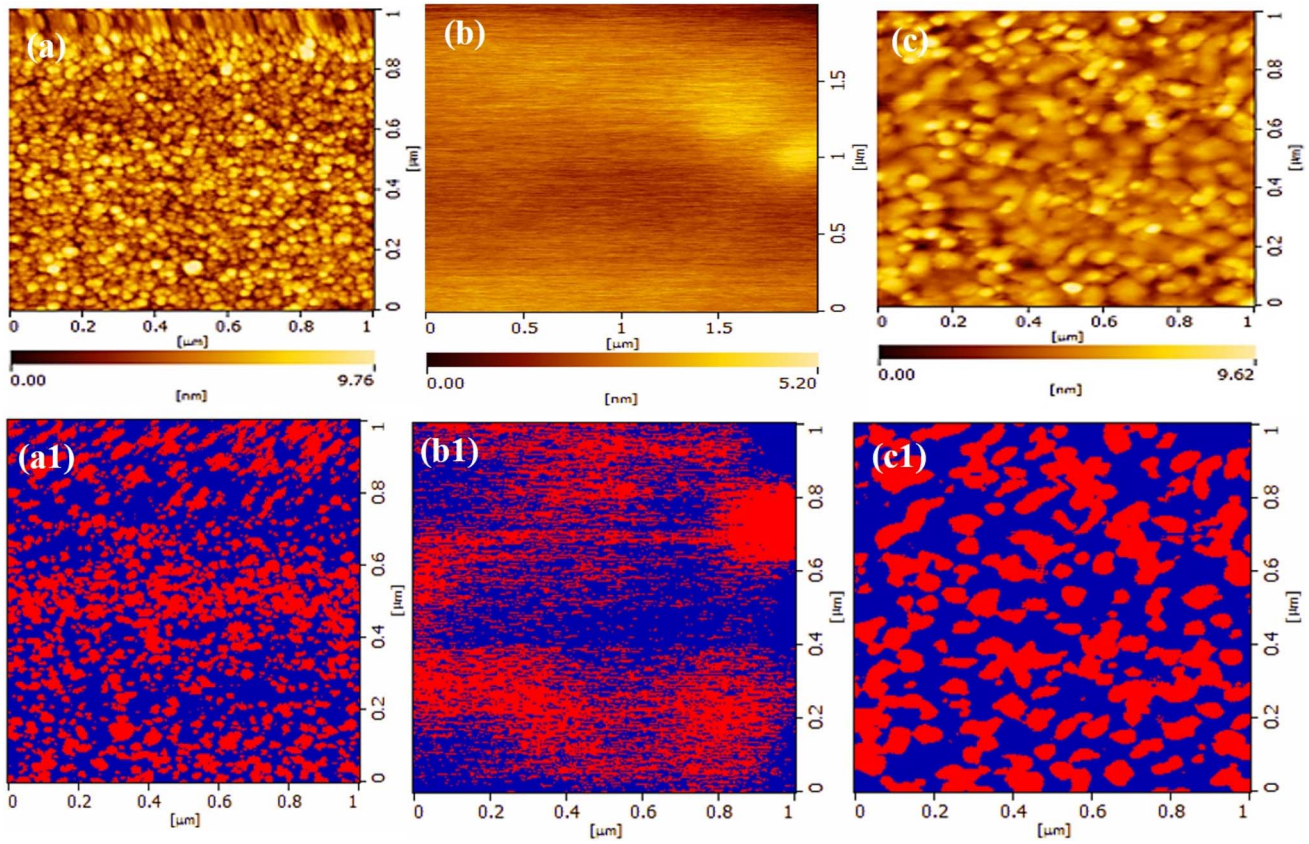

Fig. 4 Two-dimensional atomic force microscope images and grain size analysis images of the WO_3 microwires fabricated at (a and a1) 200 °C; (b and b1) 400 °C; and (c and c1) 600 °C.

lower temperatures, which promotes grain aggregation. The granular surface is expected to offer a high density of surface-active sites, beneficial for gas sensing. Increasing the deposition temperature to 400 °C leads to a significantly smoother surface, with a reduced roughness of 5.2 nm (Fig. 4b and b1). This enhanced uniformity can be attributed to improved adatom mobility, facilitating greater surface diffusion and coalescence, thereby promoting the formation of a more continuous and uniform film. Furthermore, the smoother morphology may indicate a structural transition from the amorphous to crystalline phase, as supported by the XRD analysis. At 600 °C, the surface roughness increases again to 9.52 nm, similar to that observed at 200 °C. This rise in roughness may result from the formation of well-defined crystalline domains and thermal-induced surface restructuring at elevated temperatures. The increased crystallinity and morphological changes at this temperature are consistent with the phase evolution observed in complementary structural analyses. The grain size analysis reveals that the sample deposited at 600 °C exhibits larger and more distinct grains with well-defined boundaries and reduced grain density than samples deposited at lower temperatures (Fig. 4c and c1). The increase in the grain size is attributed to enhanced adatom mobility and extended surface diffusion lengths at elevated temperatures, which promote grain growth and coalescence during deposition.

Fig. 5 shows the X-ray photoelectron spectra of the WO_3 thin films deposited at different temperatures. The W 4f and O 1s core-level spectra of the films are shown in Fig. 5a–i. At 200 °C (Fig. 5a), the W 4f spectrum exhibits two prominent peaks at binding energies of approximately 35.5 and 37.6 eV, corresponding to the W $4f_{7/2}$ and W $4f_{5/2}$ spin–orbit components, respectively. These peaks are characteristic of the W^{5+} oxidation state, indicating that tungsten exists predominantly in the fully oxidized form.[53–58] The O 1s spectrum shows a strong peak centred at approximately 530.1 eV, which is attributed to lattice oxygen (O–W bonds) within the WO_3 matrix. A secondary peak is observed at a higher binding energy, which is typically associated with adsorbed oxygen species or hydroxyl groups.[59–61]

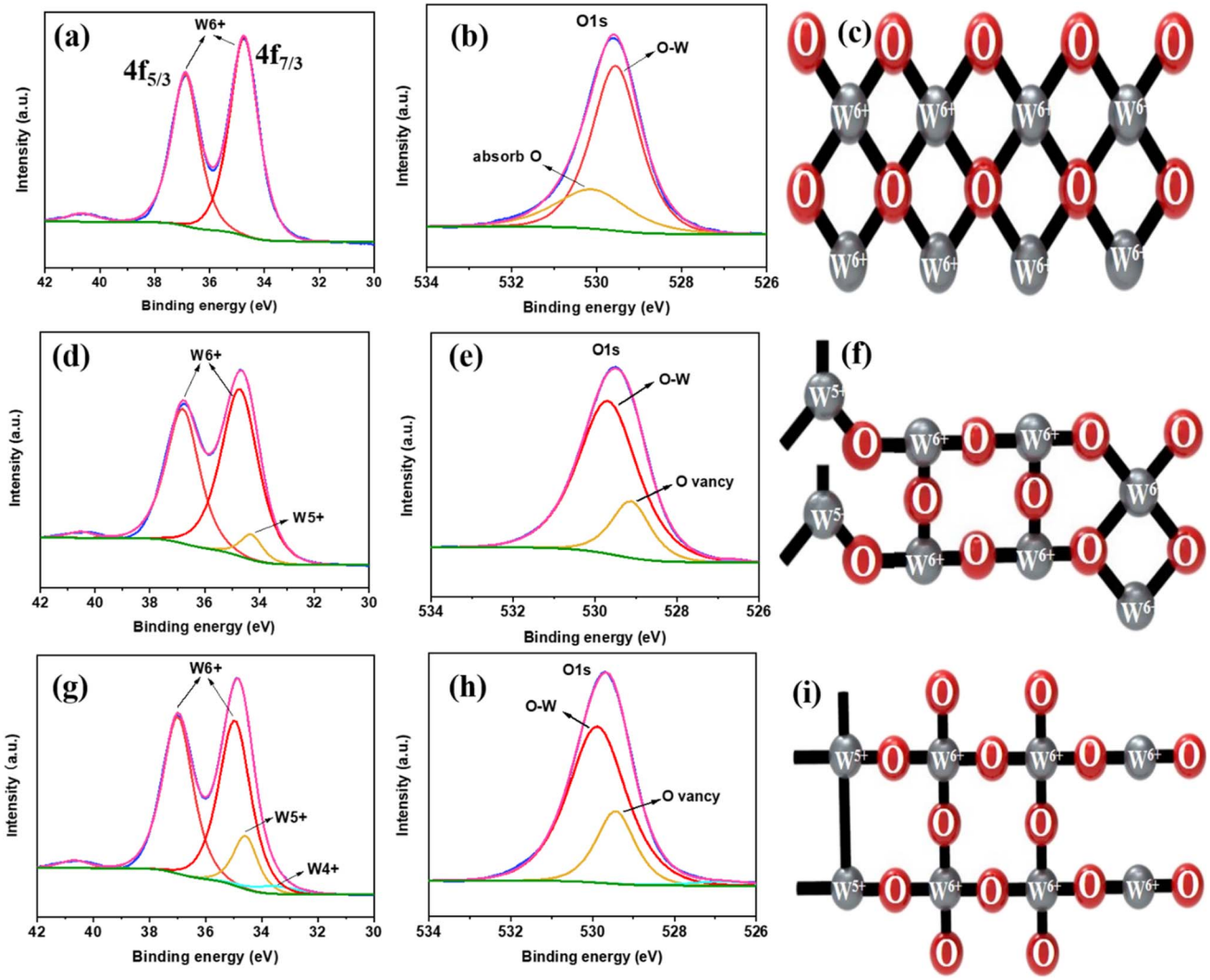

Fig. 5 W 4f and O 1s core-level spectra of the WO_3 samples prepared at (a and b) 200 °C, (d and e) 400 °C, and (g and h) 600 °C, respectively. Schematic representations of the WO_3 crystal structures at (c) 200 °C, (f) 400 °C, and (i) 600 °C.

The presence of this feature suggests the formation of a partially amorphous or defect-rich crystalline structure at this deposition temperature (Fig. 5b). The W 4f spectrum at 400 °C continues to exhibit the dominant features of the W^{6+} oxidation state; however, the peaks show slight broadening compared to those at 200 °C. Deconvolution of the spectrum reveals the presence of a minor peak at approximately 34.6 eV (W $4f_{7/2}$), corresponding to the W^{5+} oxidation state (Fig. 5d).[62,63] This indicates the presence of partially reduced tungsten species, likely arising from the formation of oxygen vacancies during deposition at elevated temperatures. The O 1s spectrum at this temperature shows a more intense lattice-oxygen peak at 530.1 eV, accompanied by the higher-binding-energy shoulder (associated with adsorbed oxygen species) with reduced intensity (Fig. 5e).

These changes suggest improved film crystallinity and a reduction in the surface defects with an increase in the deposition temperature. At 600 °C, the W 4f spectrum shows a further increase in the intensity of the W^{5+} component along with the emergence of a minor W^{4+} peak at approximately 33.4 eV (W $4f_{7/2}$).[57,58] The presence of these reduced tungsten states is indicative of an increased concentration of oxygen vacancies, which commonly form at higher deposition temperatures because of enhanced oxygen atom mobility and partial reduction of the film (Fig. 5g). The corresponding O 1s spectrum reveals a more pronounced contribution from lattice oxygen, while the intensity of the peak corresponding to adsorbed oxygen species is significantly diminished.[51,64,65] These spectral features suggest improved crystallinity and structural ordering with a higher density of lattice vacancies, further supporting the temperature-driven evolution of the film composition and microstructure (Fig. 5h). The schematic illustrations in Fig. 5c, f and i depict the temperature-dependent evolution of the crystal structure of the WO_3 thin films.

4. Gas sensing performance and mechanism

The gas sensing performance of the fabricated WO_3-based sensor toward acetone vapour was systematically investigated across a wide concentration range, from 100 ppm to 100 ppb, under dry and ambient air atmospheres. The sensor exhibits a typical n-type semiconducting response, *i.e.*, its resistance decreases when exposed to acetone, which is a reducing gas. Fig. 6a shows the gas response under dry air conditions; the resistance of the WO_3 sensor increases progressively with increase in the acetone concentration. The resistance response is clearly distinguishable at each concentration level, including sub-ppm levels. The resistance change becomes more pronounced with a sharp and consistent rise at each step, demonstrating the concentration-dependent behaviour of the gas sensor. Fig. 6b shows the sensing performance in an air atmosphere with natural humidity (~30%). The sensor exhibits a characteristic decrease in the resistance upon exposure to acetone, consistent with the typical behaviour of n-type semiconductors interacting with reducing gases. Notably, the sensor demonstrates a remarkable sensitivity even at low concentrations, down to 100 ppb in the air atmosphere. As the acetone concentration increases, the drop in the resistance becomes more pronounced and well-defined, accompanied by fast and reversible response characteristics. These results confirm the capability of the sensor to detect a wide dynamic range of acetone concentrations with high reliability. Time-resolved measurements further supported the efficiency of the sensor. As shown in Fig. 6c, exposure to 10 ppm acetone under dry air conditions results in a response time of approximately 25 s and a recovery time of 10 s. In comparison, exposure to 500 ppb acetone in ambient air leads to slightly longer response and recovery times of ~19 and ~20 s, respectively (Fig. 6d). This delay at lower concentrations is likely because of the reduced number of acetone molecules available for interaction with the sensing surface, requiring longer adsorption and desorption processes. These observations highlight the excellent potential of the WO_3-based sensor for rapid, sensitive, and reversible detection of acetone in dry and humid conditions. Fig. 6e demonstrates the WO_3 microwire gas sensor's selectivity at 300 °C, revealing a markedly higher response to acetone compared to other tested gases, including ethanol, ammonia, and acetic acid. Fig. 6f shows the baseline stability of the sensor when exposed to dry and ambient air without the presence of target gas molecules. The resistance remains nearly constant throughout the measurement period, indicating excellent baseline stability and negligible interference from the background atmosphere. This observation confirms that the sensor exhibits high selectivity and a stable response, with minimal influence from humidity or environmental fluctuations in the absence of acetone.

4.1 Gas sensing mechanism in the air atmosphere

The sensing mechanism of the WO_3-based gas sensors is explained by the electron depletion layer model, as widely reported in previous studies. When an n-type WO_3 sensor is exposed to air, oxygen molecules adsorb onto the sensor surface and extract electrons from the conduction band of WO_3, leading to the formation of chemisorbed oxygen species. The dominant adsorbed species vary with the temperature: O_2^- below 100 °C, O^- between 100–300 °C, and O^{2-} above 300 °C.[66–70] Under typical operating conditions (~300 °C), the oxygen molecules from the ambient dry air are adsorbed on the WO_3 surface and undergo ionization by extracting electrons from the conduction band of WO_3. The corresponding surface reactions can be represented as:

$$O_2(ads) + e^- \rightarrow O_2^-(ads) \quad (1)$$

$$O_2^- + e^- \rightarrow 2O^-(ads) \quad (2)$$

$$CH_3COCH_3 + O^-(ads) \rightarrow CH_3CO^{\bullet}(ads) + OH^- \quad (3)$$

$$CH_3^{\bullet} + O^-(ads) \rightarrow CH_3^{\bullet}(ads) + CO_2 \quad (4)$$

$$CH_3^{\bullet} + O^-(ads) \rightarrow CO_2 + H_2O + e^- \quad (5)$$

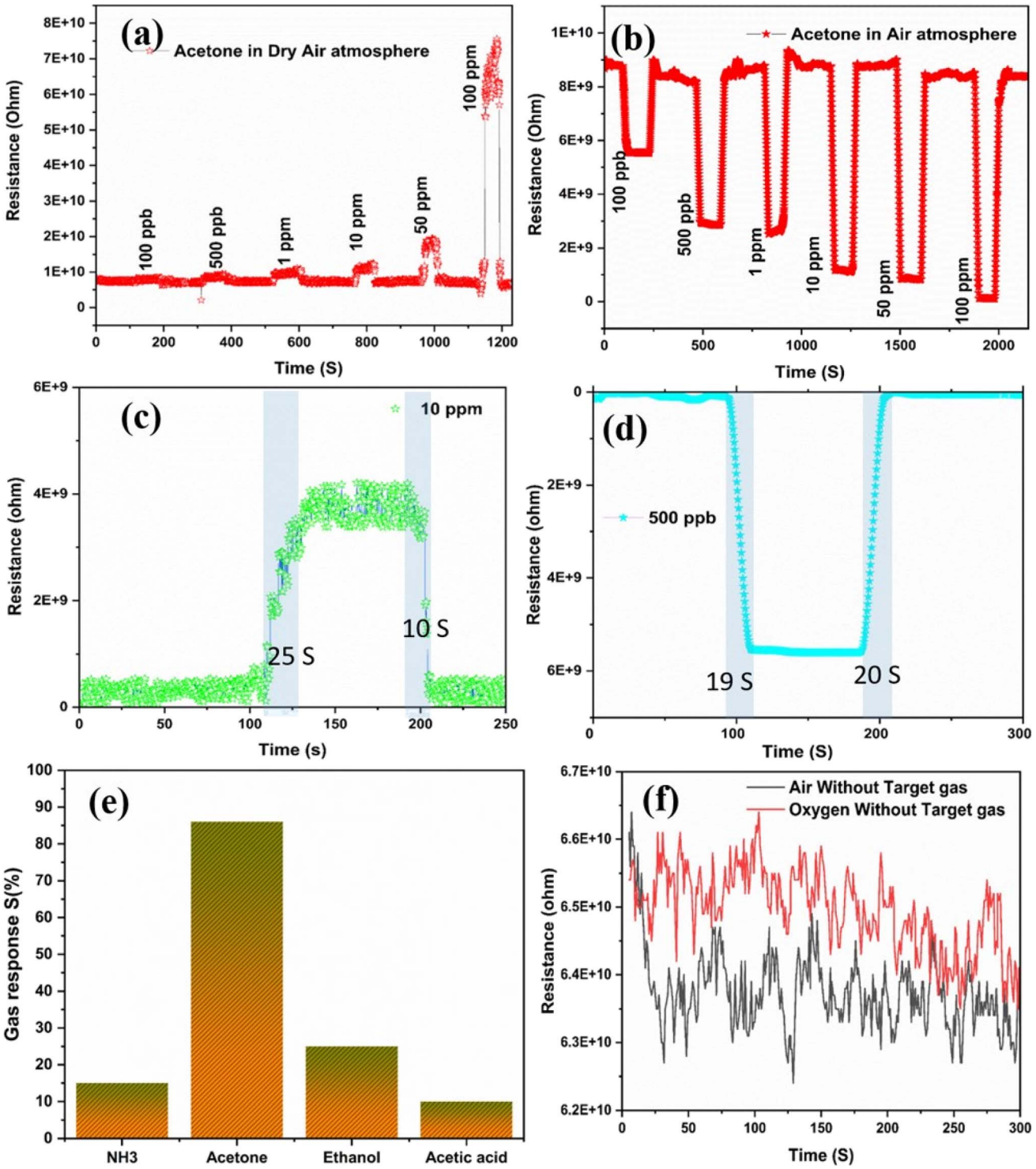

Fig. 6 Gas response and recovery plots of the a-WO_3 nanowire in (a and c) dry air and (b and d) ambient air, respectively. (e) Selectivity of gas sensor towards different gas molecules, (f) resistance of the gas sensor measured in dry and ambient air without target gas.

The accumulation of these ionized oxygen species significantly depletes the electrons near the surface, leading to upward band bending and an increase in the sensor resistance (owing to the formation of a wide depletion region).[70,71] When acetone (CH_3-$COCH_3$), a volatile organic compound, is introduced to the sensing environment, it typically acts as a reducing agent. Under ideal conditions, the acetone molecules react with the adsorbed oxygen species on the surface of WO_3, releasing electrons back into the conduction band. This decreases the resistance of the sensor.

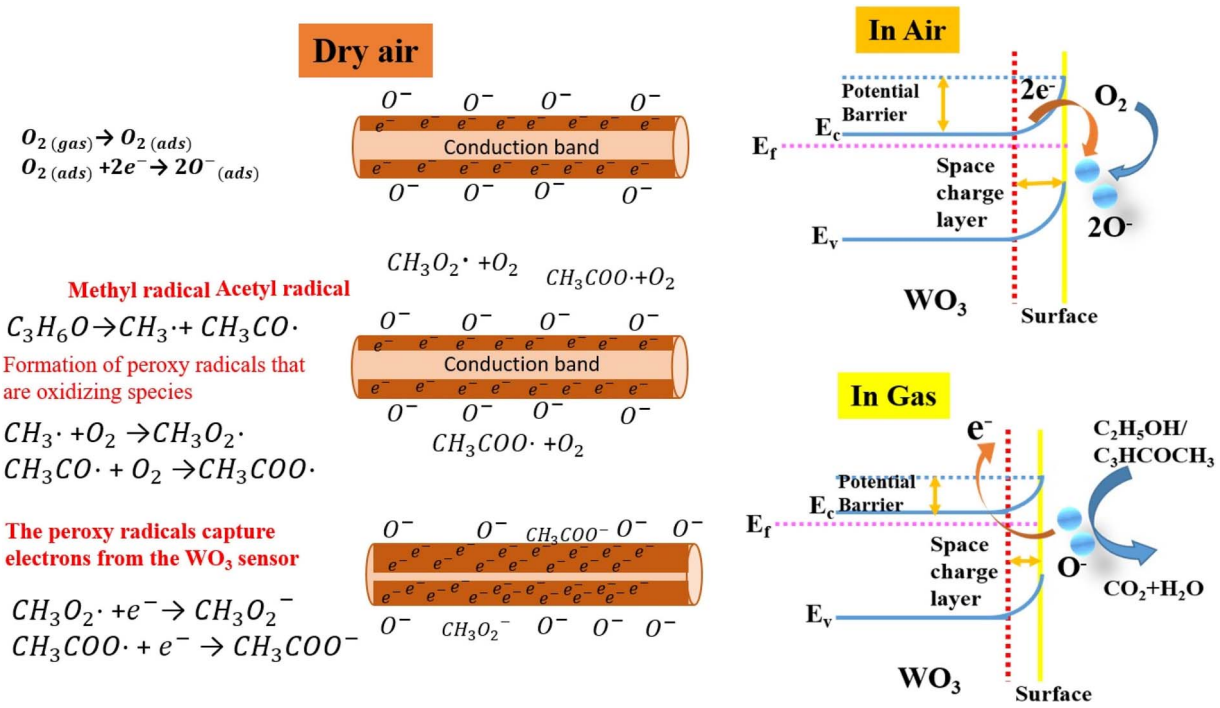

Fig. 7 Schematic of the acetone gas sensing mechanism of WO_3 in dry air and standard air atmospheres.

4.2 Gas sensing mechanism in the dry air atmosphere

In the present study, we observed an anomalous sensing response in which the resistance increased upon acetone exposure. This can be attributed to the following competing processes. (1) Excessive oxygen adsorption: under dry air and elevated temperature conditions, excessive surface oxygen coverage can result in the saturation of adsorption sites. The adsorbed oxygen species dominate the surface, making the complete oxidation of acetone energetically unfavourable.[72] (2) Incomplete oxidation or surface blocking: instead of complete mineralisation, acetone may undergo partial oxidation or become physisorbed, forming surface-bound intermediates (*e.g.*, $CH_3CO^{\bullet}$, CH_3COO^-), which either block the active sites or form dipolar layers that trap electrons. (3) Electronic and band structure effects: the formation of such intermediates alters the surface potential, leading to enhanced band bending and further increase in the width of the depletion region. This restricts electron transport through the WO_3 layer and increases the resistance. Collectively, these effects suppress the usual electron-donating behaviour of acetone and instead yield a resistance-increasing response. Such a mechanism is likely influenced by the surface morphology, crystallinity, and the nature of the oxygen species adsorbed on WO_3 and may be further modulated by humidity and dopants (Fig. 7).

5. Conclusion

In summary, WO_3 thin films were deposited on $LaAlO_3$ (100) substrates *via* pulsed laser deposition for acetone gas sensing applications. The amorphous WO_3 films, deposited at 200 °C, exhibited good sensitivity at 300 °C with a detection limit of 100 ppb. Increasing the substrate temperature to 600 °C during deposition resulted in highly crystalline WO_3 films with improved structural stability, as confirmed by XRD. The AFM analysis showed a uniform surface morphology with nanoscale grains, which played a key role in enhancing the gas adsorption. The sensor demonstrated fast response and recovery times of 19 and 20 s, respectively. The distinct sensing mechanisms observed under dry and ambient air conditions highlighted the impact of humidity and surface oxygen species on the sensor behaviour. These results emphasize the importance of deposition temperature and microstructure in optimising the gas sensing performance and support the potential of WO_3 thin films for integration into wearable, non-invasive biomedical sensing platforms.

Conflicts of interest

There are no conflicts to declare.

Data availability

The data supporting this article have been included as part of the SI.

Supplementary information: data including XRD, XPS, SEM and gas sensing analysis See DOI: **https://doi.org/10.1039/d5ra04753f**.

Acknowledgements

This research is supported by the Institute for AI and Beyond for the University of Tokyo, JST, CREST Grant Number

JPMJCR22O2, Japan, AMED under Grant Number JP22zf0127006, JSPS KAKENHI Grant Number JP20H05651, 25H00730, 25H02602, and 25K22084.

References

1 S. Das and M. Pal, Review—Non-Invasive Monitoring of Human Health by Exhaled Breath Analysis: A Comprehensive Review, *J. Electrochem. Soc.*, 2020, **167**(3), 037562, DOI: **10.1149/1945-7111/ab67a6**.

2 C. Wang and P. Sahay, Breath Analysis Using Laser Spectroscopic Techniques: Breath Biomarkers, Spectral Fingerprints, and Detection Limits, *Sensors*, 2009, **9**(10), 8230–8262, DOI: **10.3390/s91008230**.

3 H. Zhou, S. G. Ramaraj, M. S. Sarker, S. Tang, H. Yamahara and H. Tabata, Parts-per-Trillion-Level Acetone Gas Detection Using a Suspended Graphene/SiO2 SAW Breath and Skin Gas Sensor: Simulation and Experimental Study, *ACS Sens.*, 2025, **18**, 804–813, DOI: **10.1021/acssensors.4c02344**.

4 S. Miura, K. Watanabe, A. Karashima and Y. Yamada Maruo, Disulfide Compound-Impregnated Paper Substrate-Based Highly Efficient Colorimetric Gas Sensor for Detection of Volatile Sulfur Compounds in Noninvasive Breath Analysis, *ACS Sens.*, 2025, **10**, 1023–1031, DOI: **10.1021/acssensors.4c02865**.

5 X. Ma, R. Tan, H. Chen, J. Zhang, L. Ge, T. Zhao, X. Wang, K. Yuan, H. Fang and D. Wang, Smart Breath Sentinel: A NO2 Gas Sensor with Ppt-Level Detection Lower Limit and High Signal-to-Noise Ratio Based on In(OH)3-α-Fe2O3-ZnO for an Application on Intelligent Upgrade of Ordinary Masks, *ACS Sens.*, 2025, **10**(4), 2627–2639, DOI: **10.1021/acssensors.4c03131**.

6 X. Cui, H. Wang, X. Wang, Y. Tang, Y. Zhang, Y. Dong, L. Jing and L. Shen, Room Temperature and Humidity Resistant NH3 Detection Based on a Composite of Hydrophobic CNTs with Sulfur Nanosheets, *ACS Sens.*, 2025, **10**, 1756–1764, DOI: **10.1021/acssensors.4c02076**.

7 Y. Du, H. Zhang, J. Zheng, Q. Li, R. Xu, J. Xu, Y. Y. Song, P. Song, Z. Gao and C. Zhao, Integrating Vacancies and Defect Levels in Heterojunctions to Synergistically Enhance the Performance of H2S Chemiresistors for Periodontitis Diagnosis, *ACS Sens.*, 2025, **34**, 18, DOI: **10.1021/acssensors.5c00205**.

8 N. Alizadeh, H. Jamalabadi and F. Tavoli, Breath Acetone Sensors as Non-Invasive Health Monitoring Systems: A Review, *IEEE Sens. J.*, 2020, **20**(1), 5–31, DOI: **10.1109/jsen.2019.2942693**.

9 Y. Masuda and A. Uozumi, Highly Responsive Diabetes and Asthma Sensors with WO3 Nanoneedle Films for the Detection of Biogases with Low Concentrations, *NPG Asia Mater.*, 2023, **15**(1), 1–18, DOI: **10.1038/s41427-023-00515-7**.

10 Y. Chen, Y. Liu, J. Liu, Y. Li, Y. Liu, W. Zhang, L. Han, D. Wang, S. Cao, H. Liu, Q. Xie, X. Wang and M. Zhang, Porous PDMS-ZnO Wearable Gas Sensor for Acetone Biomarker Detection and Breath Analysis, *ACS Appl. Mater. Interfaces*, 2024, **16**, 62436–62445, DOI: **10.1021/acsami.4c16209**.

11 J. B. Cole and J. C. Florez, Genetics of Diabetes Mellitus and Diabetes Complications, *Nat. Rev. Nephrol.*, 2020, **16**(7), 377–390, DOI: **10.1038/s41581-020-0278-5**.

12 E. Na, S. Tao, W. Wang, J. Li, Y. Guo, R. Gao, Q. Li, F. Wang, C. Zhang and G. D. Li, Ultrasensitive Acetone Gas Sensor Based on a K/Sn-Co3O4 Porous Microsphere for Noninvasive Diabetes Diagnosis, *ACS Sens.*, 2024, **9**(11), 6148–6156, DOI: **10.1021/acssensors.4c02009**.

13 L. Jiang, C. Wang, T. Fan, S. Lv, S. Pan, P. Sun, J. Zheng, C. Zhang, F. Liu and G. Lu, Mixed Potential Type Acetone Sensor with Ultralow Detection Limit for Diabetic Ketosis Breath Analysis, *ACS Sens.*, 2024, **9**(1), 464–473, DOI: **10.1021/acssensors.3c02253**.

14 W. Satoshi, M. Yoshitake, C. Pil Gyu, M. Takumi, H. Yota and T. Seiichi, Semiconductor-Type Gas Sensors Based on Surface-Modified Iron Oxide Nanoparticles for ppb-Level Detection of Acetone, *ACS Appl. Electron. Mater.*, 2025, DOI: **10.1021/acsaelm.5c01355**.

15 S. M. Majhi, A. Ali, Y. E. Greish, H. F. El-Maghraby, N. N. Qamhieh, A. R. Hajamohideen and S. T. Mahmoud, Accordion-like-Ti3C2MXene-Based Gas Sensors with Sub-Ppm Level Detection of Acetone at Room Temperature, *ACS Appl. Electron. Mater.*, 2022, **4**(8), 4094–4103, DOI: **10.1021/acsaelm.2c00717**.

16 Z. Su, Z. Zhao, G. Jin, W. Chen, X. Shen and L. Wu, Enhanced Acetone Gas Sensors Based on Pt-Modified Co3O4/CoMoO4 Heterojunctions, *Phys. E*, 2024, **164**, 116042, DOI: **10.1016/j.physe.2024.116042**.

17 L. A. Siddig, A. Ali, S. S. Al Neyadi, Y. E. Greish, S. Wuttke and S. T. Mahmoud, Acetone Gas Sensor Based on Chitosan-Metal-Organic Framework Mixed Matrix Membranes for Diabetes Diagnosis, *Carbohydr. Polym. Technol. Appl.*, 2025, **9**, 100661, DOI: **10.1016/j.carpta.2025.100661**.

18 L. Li, Q. Diao, Z. Liu, G. Zhu, M. Jiao, C. Liu, M. Du, Y. Shi, Y. Wang, P. Cheng and X. Xu, Preparation of Co3O4 by Tunable Oxygen Defect Engineering and Its Application in Acetone Gas Sensor, *Microchem. J.*, 2025, **212**, 113481, DOI: **10.1016/j.microc.2025.113481**.

19 H. Su, Y. Guan, K. Zhou, C. Ma, Z. Hua, X. Wang, X. Guo and D. Zeng, Ultrasensitive Response and Ultralow Detection Limit of the Acetone Gas Sensor Based on 2D Porous Pd-Doped WO3 Nanosheets, *Ceram. Int.*, 2025, **51**(18), 25052–25062, DOI: **10.1016/j.ceramint.2025.03.187**.

20 N. H. Hanh, L. V. Duy, C. M. Hung, C. T. Xuan, N. V. Duy and N. D. Hoa, High-Performance Acetone Gas Sensor Based on Pt–Zn2SnO4 Hollow Octahedra for Diabetic Diagnosis, *J. Alloys Compd.*, 2021, **886**, 161284, DOI: **10.1016/j.jallcom.2021.161284**.

21 C. Shi, L. Yu, X. He, Y. Zhang, J. Liu, S. Li, C. Zhang, L. Cao, N. Nan, H. Du and M. Yin, Vertically Aligned Mesoporous Ce Doped NiO Nanowalls with Multilevel Gas Channels for High-Performance Acetone Gas Sensors, *Sens. Actuators, B*, 2024, **401**, 134888, DOI: **10.1016/j.snb.2023.134888**.

22 L. H. Kathwate, A. D. Kanwate, Y. P. Sarnikar, H. M. Rakhade, A. Kore, N. S. Barse and A. C. Mendhe,

Fabrication of Ni-Doped ZnO Thin Films via Spray Pyrolysis Method towards Highly Selective and Sensitive Acetone Gas Sensing, *Inorg. Chem. Commun.*, 2025, **175**, 114152, DOI: 10.1016/j.inoche.2025.114152.

23 H. Zhou, S. G. Ramaraj, K. Ma, M. S. Sarker, Z. Liao, S. Tang, H. Yamahara and H. Tabata, Real-Time Detection of Acetone Gas Molecules at Ppt Levels in an Air Atmosphere Using a Partially Suspended Graphene Surface Acoustic Wave Skin Gas Sensor, *Nanoscale Adv.*, 2023, **5**(24), 6999–7008, DOI: 10.1039/d3na00914a.

24 L. Fu, J. Xu, Q. Liu, C. Liu, S. Fan, S. Ramakrishna and W. Tang, Gas Sensors Based on Co3O4/TiO2 Core-Shell Nanofibers Prepared by Coaxial Electrospinning for Breath Marker Acetone Detection, *Ceram. Int.*, 2024, **50**(2), 3443–3452, DOI: 10.1016/j.ceramint.2023.11.092.

25 T. Yu, X. Meng, X. Hao, Z. Dong, Y. Wang, S. Sun and P. Cheng, YSZ-Based Mixed-Potential Acetone Sensor with LaBaCo2O5+δ Sensitive Electrode for Diabetic Diagnosis, *Sens. Actuators, B*, 2024, **418**, 136273, DOI: 10.1016/j.snb.2024.136273.

26 S. R. Ananda, L. Kumari and M. V. Murugendrappa, Studies on Room-Temperature Acetone Sensing Properties of ZnCo2O4/PPy and MnCo2O4/PPy Nanocomposites for Diabetes Diagnosis, *Appl. Phys. A:Mater. Sci. Process.*, 2022, **128**(8), 1–10, DOI: 10.1007/s00339-022-05792-7.

27 Q. Junwei, X. Kai, Z. Tao, Z. Huijun, Z. Shuo, L. Xinxin and L. Xiaoxu, Development of a Portable Gas Chromatography Linear Ion Trap Mass Spectrometer (GC-LIT-MS) for VOCs Analysis in Water, *Int. J. Mass Spectrom.*, 2024, **497**, 117189, DOI: 10.1016/j.ijms.2023.117189.

28 Y. n. Wang, J. Li, Z. Yuan and F. Meng, Performance Demonstration Experiment and DFT Mechanism for an Optical Fiber Toluene Gas Sensor Based on CQDs@SiO2(-OH) Porous Film, *Chem. Eng. J.*, 2025, **512**, 162153, DOI: 10.1016/j.cej.2025.162153.

29 C. Qu, H. Fang, F. Yu, J. Chen, M. Su and H. Liu, Artificial Nose of Scalable Plasmonic Array Gas Sensor for Multi-Dimensional SERS Recognition of Volatile Organic Compounds, *Chem. Eng. J.*, 2024, **482**, 148773, DOI: 10.1016/j.cej.2024.148773.

30 Y. Chang, P. Wang, J. Li, F. Yang, T. Hao and J. Pu, Performance Improvement of NiO/YSZ Sensitive Electrode for High Temperature Electrochemical NOx Gas Sensors, *Ceram. Int.*, 2024, **50**(20), 39347–39357, DOI: 10.1016/j.ceramint.2024.07.307.

31 M. Z. Aslam, H. Zhang, M. Good, Y. Guo and M. A. Larche, Multimodal Lithium Niobate-Based SAW Gas Sensor for Accurate Detection of Carbon Dioxide at Elevated Temperature, *Ultrasonics*, 2024, **138**, 107198, DOI: 10.1016/j.ultras.2023.107198.

32 S. A. Jadhav, G. Umadevi, M. B. Awale, K. S. Kanse, Y. S. Joshi, Y. Purushotham, S. D. Lokhande and V. D. Mote, Optimizing Ammonia Gas Sensor Performance: Investigating the Influence of Mg Doped ZnO Root like Nanostructures for Enhanced Gas Sensing Application, *Mater. Lett.*, 2025, **389**, 138343, DOI: 10.1016/j.matlet.2025.138343.

33 G. Dhanraj, O. Raina, M. Surendar, S. Gopinath, M. A. Manthrammel and M. Shkir, Stable and Cost-Effective La-Doped WO3 Nanoparticles for Photocatalytic Degradation of Organic and Antibiotic Pollutants under Visible Light, *Ceram. Int.*, 2025, **51**(11), 15030–15042, DOI: 10.1016/j.ceramint.2025.01.296.

34 Y. Wang, J. Li, D. Zhang, Y. Liu, T. Zhou, M. Sun, S. Chen and M. Sun, Ag Nanoparticles Modified WO3 Nanospheres Structurally Designed by NaBH4 Have High Sensitivity and Selectivity for H2S Detection at Room Temperature, *Ceram. Int.*, 2025, **51**(9), 12175–12184, DOI: 10.1016/j.ceramint.2025.01.069.

35 M. Righettoni, A. Tricoli and S. E. Pratsinis, Si:WO3 Sensors for Highly Selective Detection of Acetone for Easy Diagnosis of Diabetes by Breath Analysis, *Anal. Chem.*, 2010, **82**(9), 3581–3587, DOI: 10.1021/ac902695n.

36 Q. Wang, X. Cheng, Y. Wang, Y. Yang, Q. Su, J. Li, B. An, Y. Luo, Z. Wu and E. Xie, Sea Urchins-like WO3 as a Material for Resistive Acetone Gas Sensors, *Sens. Actuators, B*, 2022, **355**, 131262, DOI: 10.1016/j.snb.2021.131262.

37 B. Liu, D. Hong, L. Li, T. Su, L. Che, X. L. Yang, N. Xu, L. Yue and W. Zhang, Tartaric Acid-Assisted Synthesis and Acetone Gas Sensing Properties of Hierarchical WO3 Phase Junctions, *Sens. Actuators, B*, 2025, **441**, 137965, DOI: 10.1016/j.snb.2025.137965.

38 L. Wang, A. Teleki, S. E. Pratsinis and P. I. Gouma, Ferroelectric WO3 Nanoparticles for Acetone Selective Detection, *Chem. Mater.*, 2008, **20**(15), 4794–4796, DOI: 10.1021/cm800761e.

39 O. O. Abe, Z. Qiu, J. R. Jinschek and P. I. Gouma, Effect of (100) and (001) Hexagonal WO3 Faceting on Isoprene and Acetone Gas Selectivity, *Sensors*, 2021, **21**(5), 1690, DOI: 10.3390/s21051690.

40 S. J. Choi, S. Chattopadhyay, J. J. Kim, S. J. Kim, H. L. Tuller, G. C. Rutledge and I. D. Kim, Coaxial Electrospinning of WO3 Nanotubes Functionalized with Bio-Inspired Pd Catalysts and Their Superior Hydrogen Sensing Performance, *Nanoscale*, 2016, **8**(17), 9159–9166, DOI: 10.1039/c5nr06611e.

41 J. y. Leng, X. j. Xu, N. Lv, H. t. Fan and T. Zhang, Synthesis and Gas-Sensing Characteristics of WO3 Nanofibers via Electrospinning, *J. Colloid Interface Sci.*, 2011, **356**(1), 54–57, DOI: 10.1016/j.jcis.2010.11.079.

42 M. Yin, L. Yu and S. Liu, Synthesis of Thickness-Controlled Cuboid WO3 Nanosheets and Their Exposed Facets-Dependent Acetone Sensing Properties, *J. Alloys Compd.*, 2017, **696**, 490–497, DOI: 10.1016/j.jallcom.2016.11.149.

43 A. Labidi, C. Jacolin, M. Bendahan, A. Abdelghani, J. Guérin, K. Aguir and M. Maaref, Impedance Spectroscopy on WO3 Gas Sensor, *Sens. Actuators, B*, 2005, **106**(2), 713–718, DOI: 10.1016/j.snb.2004.09.022.

44 X. Y. Yang, H. N. Chen, L. J. Yue, F. L. Gong, K. F. Xie, S. Z. Wei and Y. H. Zhang, Surface Engineering of 1D Na-Doped Pd/WO3 Nanorods for Chemiresistive H2 Sensing, *Sens. Actuators, B*, 2025, **423**, 136825, DOI: 10.1016/j.snb.2024.136825.

45 B. An, Y. Yang, J. Yan, Y. Wang, R. Li, Z. Wu, T. Zhang, R. Han, X. Cheng, Q. Wang and E. Xie, Oxygen Vacancies Engineering and Palladium Quantum Dots Sensitized WO3 Nanosheet for Highly Efficiently H2 Detection, *Appl. Surf. Sci.*, 2025, **692**, 162722, DOI: 10.1016/j.apsusc.2025.162722.

46 J. Ding, M. Xie, Z. Li and Y. Wang, Fabrication of WO3 Nanosheets with Hexagonal/Orthorhombic Homojunctions for Highly Sensitive Ozone Gas Sensors at Low Temperature, *J. Alloys Compd.*, 2025, **1010**, 178228, DOI: 10.1016/j.jallcom.2024.178228.

47 A. Xu, Y. Zhang, H. Fan, X. Liu, F. Wang, X. Qu, L. Yang, X. Li, J. Cao and M. Wei, WO3 Nanosheet/ZnIn2S4 S-Scheme Heterojunctions for Enhanced CO2 Photoreduction, *ACS Appl. Nano Mater.*, 2024, **7**(3), 3488–3498, DOI: 10.1021/acsanm.4c00147.

48 Y. Sun, B. Du, Y. Wang, M. Zhang and S. Zhang, Hydrogen Spillover-Accelerated Selective Hydrogenation on WO3 with Ppm-Level Pd, *ACS Appl. Mater. Interfaces*, 2023, **15**(16), 20474–20482, DOI: 10.1021/acsami.3c00456.

49 A. K. Mohamedkhair, Q. A. Drmosh, M. Qamar and Z. H. Yamani, Tuning Structural Properties of WO3 Thin Films for Photoelectrocatalytic Water Oxidation, *Catal*, 2021, **11**(3), 381, DOI: 10.3390/catal11030381.

50 M. Wang, S. Shen, J. Ni, N. Lu, Z. Li, H. B. Li, S. Yang, T. Chen, J. Guo, Y. Wang, H. Xiang and P. Yu, Electric-Field-Controlled Phase Transformation in WO3 Thin Films through Hydrogen Evolution, *Adv. Mater.*, 2017, **29**(46), 1703628, DOI: 10.1002/adma.201703628.

51 A. Herklotz, S. F. Rus, S. Kc, V. R. Cooper, A. Huon, E. J. Guo and T. Z. Ward, Symmetry Driven Control of Optical Properties in WO3 Films, *APL Mater.*, 2017, **5**(6), 49, DOI: 10.1063/1.4989395/121476.

52 Z. j. Xia, H. l. Wang, Y. f. Su, P. Tang, M. j. Dai, H. j. Lin, Z. g. Zhang and Q. Shi, Enhanced Electrochromic Properties by Improvement of Crystallinity for Sputtered WO3 Film, *Coatings*, 2020, **10**(6), 577, DOI: 10.3390/coatings10060577.

53 J. T. Yang, C. Ma, C. Ge, Q. H. Zhang, J. Y. Du, J. K. Li, H. Y. Huang, M. He, C. Wang, S. Meng, L. Gu, H. B. Lu, G. Z. Yang and K. J. Jin, Effects of Line Defects on the Electronic and Optical Properties of Strain-Engineered WO 3 Thin Films, *J. Mater. Chem. C*, 2017, **5**(45), 11694–11699, DOI: 10.1039/c7tc03896h.

54 M. Tong, J. Yang, Q. Jin, X. Zhang, J. Gao and G. Li, Facile Preparation of Amorphous Carbon-Coated Tungsten Trioxide Containing Oxygen Vacancies as Photocatalysts for Dye Degradation, *J. Mater. Sci.*, 2019, **54**(15), 10656–10669, DOI: 10.1007/s10853-019-03645-y.

55 K. M. McCreary, A. T. Hanbicki, G. G. Jernigan, J. C. Culbertson and B. T. Jonker, Synthesis of Large-Area WS2 Monolayers with Exceptional Photoluminescence, *Sci. Rep.*, 2016, **6**(1), 1–7, DOI: 10.1038/srep19159.

56 Y. Shao, D. You, Y. Wan, Q. Cheng and Z. Pan, An Investigation on a WO 3/MoO 3−x Heterojunction Photocatalyst for Excellent Photocatalytic Performance and Enhanced Molecular Oxygen Activation Ability, *React. Chem. Eng.*, 2023, **9**(1), 70–81, DOI: 10.1039/d3re00396e.

57 L. Sharma, P. Kumar and A. Halder, Phase and Vacancy Modulation in Tungsten Oxide: Electrochemical Hydrogen Evolution, *ChemElectroChem*, 2019, **6**(13), 3420–3428, DOI: 10.1002/celc.201900666.

58 Z. Zhang, J. Liang, K. Liu, W. Tian, X. Liang, K. Zhao and K. Zhang, Defect-Engineered WO3-x Architectures Coupled with Random Forest Algorithm Enables Real-Time Seafood Quality Assessment, *ACS Sens.*, 2024, **9**(8), 4196–4206, DOI: 10.1021/acssensors.4c01192.

59 H. Lin, J. Wang, S. Xu, Q. Zhang, Y. Cheng, D. Han, H. Wang and K. Zhuo, Au-WO3 Nanowire-Based Electrodes for NO2Sensing, *ACS Appl. Nano Mater.*, 2022, **5**(10), 14311–14319, DOI: 10.1021/acsanm.2c02289.

60 B. An, Y. Yang, Y. Wang, R. Li, Z. Wu, P. Wang, T. Zhang, R. Han and E. Xie, Observation on Switching Properties of WO3-Based H2 Sensor Regulated by Temperature and Gas Concentration, *ACS Sens.*, 2024, **58**, 32, DOI: 10.1021/acssensors.4c01212.

61 F. Bussolotti, H. Kawai, T. D. Maddumapatabandi, W. Fu, K. H. Khoo and K. E. J. Goh, Role of S-Vacancy Concentration in Air Oxidation of WS2 Single Crystals, *ACS Nano*, 2024, **18**(12), 8706–8717, DOI: 10.1021/acsnano.3c10389.

62 S. Watmanee, K. Suriye, P. Praserthdam and J. Panpranot, Effect of Surface Tungstate W5+ Species on the Metathesis Activity of W-Doped Spherical Silica Catalysts, *Top. Catal.*, 2018, **61**(15–17), 1615–1623, DOI: 10.1007/s11244-018-1020-4.

63 A. Romanyuk, V. Melnik and P. Oelhafen, Oxidation of Tungsten Surface with Reactive Oxygen Plasma, *Nucl. Instrum. Methods Phys. Res., Sect. B*, 2005, **232**(1–4), 358–361, DOI: 10.1016/j.nimb.2005.03.073.

64 R. Sankar ganesh, M. Navaneethan, G. K. Mani, S. Ponnusamy, K. Tsuchiya, C. Muthamizhchelvan, S. Kawasaki and Y. Hayakawa, Influence of Al Doping on the Structural, Morphological, Optical, and Gas Sensing Properties of ZnO Nanorods, *J. Alloys Compd.*, 2017, **698**, 555–564, DOI: 10.1016/j.jallcom.2016.12.187.

65 R. Sankar Ganesh, M. Navaneethan, V. L. Patil, S. Ponnusamy, C. Muthamizhchelvan, S. Kawasaki, P. S. Patil and Y. Hayakawa, Sensitivity Enhancement of Ammonia Gas Sensor Based on Ag/ZnO Flower and Nanoellipsoids at Low Temperature, *Sens. Actuators, B*, 2018, **255**, 672–683, DOI: 10.1016/j.snb.2017.08.015.

66 Q. Liao, Q. Sun, C. Cao, J. Hu, Y. Wang, S. Li, J. Xu, G. Li, Y. Zhu and D. Wang, One-Dimensional Hierarchical Core-Shell Metal Oxide Semiconductor@WO3 Nanocomposites for Ppb-Level Acetone Sensing, *Sens. Actuators, B*, 2024, **415**, 136008, DOI: 10.1016/j.snb.2024.136008.

67 J. Ding, Z. Li, Y. Wang, Y. Liu, F. Li, X. Yu, P. Huang and Y. Wang, Ir Doping Improved Oxygen Activation of WO3 for Boosting Acetone Sensing Performance at Low Working Temperature, *Appl. Surf. Sci.*, 2025, **679**, 161239, DOI: 10.1016/j.apsusc.2024.161239.

68 Y. Zhang, W. He, H. Zhao and P. Li, Template-Free to Fabricate Highly Sensitive and Selective Acetone Gas

Sensor Based on WO3 Microspheres, *Vacuum*, 2013, **95**, 30–34, DOI: **10.1016/j.vacuum.2013.02.005**.

69 Y. Haiduk, A. Khort, V. Lapitskaya, T. Kuznetsova, D. Moskovskikh, A. Savitsky, N. Lapchuk, M. Makhavikou and V. Pankov, WO3–Graphene–Cu Nanocomposites for CO, NO2 and Acetone Gas Sensors, *Nano-Struct. Nano-Objects*, 2022, **29**, 100824, DOI: **10.1016/j.nanoso.2021.100824**.

70 Q. Wang, X. Cheng, Y. Wang, Y. Yang, Q. Su, J. Li, B. An, Y. Luo, Z. Wu and E. Xie, Sea Urchins-like WO3 as a Material for Resistive Acetone Gas Sensors, *Sens. Actuators, B*, 2022, **355**, 131262, DOI: **10.1016/j.snb.2021.131262**.

71 A. Stanoiu, I. D. Vlaicu, A. C. Iacoban, C. G. Mihalcea, C. Ghica, O. G. Florea, I. V. Dinu, I. Mercioniu and C. E. Simion, Low Traces of Acetone Detection with WO3-Based Chemical Sensors, *Mater. Chem. Phys.*, 2024, **316**, 129105, DOI: **10.1016/j.matchemphys.2024.129105**.

72 K. Kim, P. g. Choi, T. Itoh and Y. Masuda, Atomic Step Formation on Porous ZnO Nanobelts: Remarkable Promotion of Acetone Gas Detection up to the Parts per Trillion Level, *J. Mater. Chem. A*, 2022, **10**(26), 13839–13847, DOI: **10.1039/d2ta02789e**.